

# Beam Dynamics Driven Design of PERLE

S.A. Bogacz\*

*Center for Advanced Studies of Accelerators,  
Jefferson Lab, Newport News, USA*

K.D.J. André,<sup>†</sup> O. Brüning, and B.J. Holzer  
*CERN, Meyrin, Switzerland*

B.R. Hounsell<sup>‡</sup> and M. Klein  
*University of Liverpool, Liverpool, United Kingdom*

B.L. Milityn<sup>§</sup> and P.H. Williams<sup>§</sup>  
*STFC Daresbury Laboratory, Sci-Tech Daresbury, Warrington, United Kingdom*

G. Pérez Segurana,<sup>¶</sup> I. Bailey,<sup>§</sup> R. Apsimon,<sup>§</sup> and S. Setiniyaz\*\*  
*Lancaster University, Bailrigg, Lancaster, United Kingdom*

R. Abukeshek, C. Barbagallo,<sup>¶</sup> M. Ben Abdillah, C. Bruni, P. Duchesne, P. Duthil, A. Fomin, C. Guyot, W. Kaabi, J. Michaud, G. Olry, L. Perrot, D. Reynet, R. Roux, A. Stocchi, and S. Wurth  
*Université Paris-Saclay, CNRS/IN2P3 IJCLab, Orsay, France*

H. Abualrob<sup>††</sup>  
*An-Najah National University, Nablus, Palestine*

M. Baylac and F. Bouly  
*Laboratoire de Physique Subatomique et de Cosmologie (LPSC) Université Grenoble-Alpes, CNRS/IN2P3, France*

B. Jacquot  
*Grand Accélérateur Nat. d'Ions Lourds (GANIL), France*  
(Dated: June 19, 2024)

PERLE (Powerful ERL for Experiments) is a novel Energy Recovery Linac (ERL) test facility [1], designed to validate choices for a 50 GeV ERL foreseen in the design of the Large Hadron Electron Collider (LHeC) and the Future Circular Collider (FCC-eh), and to host dedicated nuclear and particle physics experiments. Its main goal is to demonstrate high current, continuous wave (CW), multi-pass operation with superconducting cavities at 802 MHz. With very high beam power (10 MW), PERLE offers an opportunity for controllable study of every beam dynamic effect of interest in the next generation of ERLs and becomes a ‘stepping stone’ between present state-of-art 1 MW ERLs and future 100 MW scale applications.

## I. INTRODUCTION

Next generation colliders [2, 3], or light sources would greatly benefit from recirculated and energy recovered linacs. They offer CW, or other high duty factor operation, high average beam current, low delivered beam

energy spread, and low delivered beam emittance. CW beam acceleration with high accelerating gradient (20 - 30 MV/m) generally requires a multi-pass Recirculating Linear Accelerator (RLA) consisting of superconducting accelerator structures. GeV-scale RLAs at 100 mA average current would ordinarily require at least 100 MW of installed RF power merely to accelerate the beam load. Energy recovery allows the RF beam loading of the cavities to be substantially lowered, thereby providing linac quality/brightness beam at storage ring beam powers. This production of high beam power with reduced RF drive represents improved electrical efficiency, representing a step change in the sustainability of electron accelerator based facilities. Particularly, the PERLE facility, to be hosted at Irène Joliot Curie Laboratory, targets the LHeC configuration and beam currents of up to 20 mA (corresponding to a 120 mA cavity load). This unique quality beam will be exploited to perform a number of

---

\* bogacz@jlab.org

<sup>†</sup> also at University of Liverpool, Liverpool, United Kingdom

<sup>‡</sup> also at IJCLab, CNRS/IN2P3 Université Paris-Saclay, Orsay, France; also at Cockcroft Institute, Warrington, United Kingdom; now at STFC Daresbury Laboratory, Warrington, United Kingdom

<sup>§</sup> also at Cockcroft Institute, Warrington, United Kingdom

<sup>¶</sup> now at CERN, Geneva, Switzerland

\*\* now at Jefferson Lab, Newport News, USA

<sup>††</sup> also at IJCLab, CNRS/IN2P3 Université Paris-Saclay, Orsay, France

experiments in different fields; ranging from uncharted tests of accelerator components via elastic ep scattering to laser-Compton back-scattering for photon physics [4]. Following an experiment at full 3-pass energy, the CW beam will be decelerated in three consecutive passes back to the injection energy, transferring virtually stored energy back to the RF.

TABLE I: PERLE Beam Parameters

| Parameter                              | Unit    | Value  |
|--|---------|--------|
| Injection beam energy                  | MeV     | 7      |
| Number of passes                       |         | 3      |
| Energy per linac                       | MeV     | 82.2   |
| Norm. emittance $\gamma\epsilon_{x,y}$ | mm·mrad | 6      |
| Average beam current                   | mA      | 20     |
| Cavity load current                    | mA      | 120    |
| Bunch charge                           | pC      | 500    |
| Bunch length                           | mm      | 1.5    |
| Bunch spacing                          | ns      | 24.95  |
| RF frequency                           | MHz     | 801.58 |
| Duty factor                            |         | CW     |

## II. LATTICE ARCHITECTURE AND OPTICS

The PERLE accelerator complex is arranged in a race-track configuration hosting two cryomodules containing four, 5-cell, cavities operating at 802 MHz each located in one of two parallel straights. The three recirculating arcs on each side are separated vertically with 45 cm between them. Additional space is taken by 4-6 meter long spreaders/recombiners including matching sections, and two experimental areas as illustrated in Fig. 1. A Flexible Momentum Compaction (FMC) lattice architecture [5] is utilised for the six arcs. Starting with a high current (in excess of 20 mA) 7 MeV photo-injector, a final energy of 500 MeV can be reached in three re-circulation passes assuming two 4-cavity cryomodules. Each cryomodule provides an 82.2 MeV energy boost per turn. Initially, CERN SPL cryomodules were considered however a decision has been made to use the Lund ESS cryomodule design as it provides greater space for HOM couplers. A summary of design parameters is presented in Table I, these have been chosen to match those of the LHeC [6], so that it will serve as a test bed for its ERL design and SRF technology development. The bunch spacing will be 25 ns, however empty bunches might be required in the LHeC ERL for ion clearing gaps.

### A. Multi-pass Linac Optics with Energy Recovery

Injection at 7 MeV into the first linac is achieved by a fixed field injection chicane, with its last magnet being placed at the beginning of the linac. This closes the orbit ‘bump’ at injection, but the magnet will deflect the beam on all subsequent passes. In order to close the resulting

higher pass bumps, a ‘re-injection’ chicane is arranged by placing two additional opposing bends in front of the last chicane magnet. The injection pass optics is illustrated in Fig. 2, with the top insert depicting the SPL cryo-module layout. The second linac in the racetrack is configured exactly as a mirror image of the first with a replica of the re-injection chicane at its end which performs a fixed-field extraction of the energy recovered beam to the dump at 7 MeV.

Multi-pass energy recovery in a racetrack topology with identical energies at each pass for accelerating and decelerating beam requires that they share individual return arcs. This imposes specific requirements for the optics at the linac ends: the Twiss functions have to be identical for both the accelerating and decelerating linac passes converging to the same energy and therefore entering the same arc. To represent beta functions for multiple accelerating and decelerating passes through a given linac it is convenient to reverse the linac direction for all decelerating passes and string them together with the interleaved accelerating passes, as illustrated in Fig. 3. This way the corresponding accelerating and decelerating passes are joined together at the arcs entrance/exit, automatically satisfying the matching conditions into the arcs.

### B. Recirculating Arcs

The spreaders are placed directly after each linac to separate beams of different energies and to route them to the corresponding arcs. The recombiners facilitate the opposite: merging the beams of different energies into the same trajectory before entering the next linac. Each spreader starts with a vertical bending magnet that initiates the separation. The highest energy, at the bottom, is brought back to the initial linac level with a chicane. The lower energies are captured with a two-step vertical beam line. The vertical dispersion introduced by the first step bends is suppressed by the three quadrupoles located appropriately between the two steps. The lowest energy spreader is configured with three curved bends following the common magnet, necessary because of the large bending angle ( $30^\circ$ ). This minimizes the adverse effects of strong edge focusing on the dispersion suppression. Following the spreader there are four matching quads to bridge the optics between the spreader and the following arc. All six arcs are configured with a FMC style optics to ease individual adjustment of the momentum compaction factor in each arc. This is required to allow a self-consistent longitudinal match for the entire system, described in Section IV. The arcs are now composed of 6 dipoles instead of a previous design iteration [1]. This increased number of dipoles allows reduction of emittance increase due to Coherent Synchrotron Radiation (CSR) [7]. The low energy implies that the energy spread and emittance growth due to incoherent synchrotron radiation is negligible.

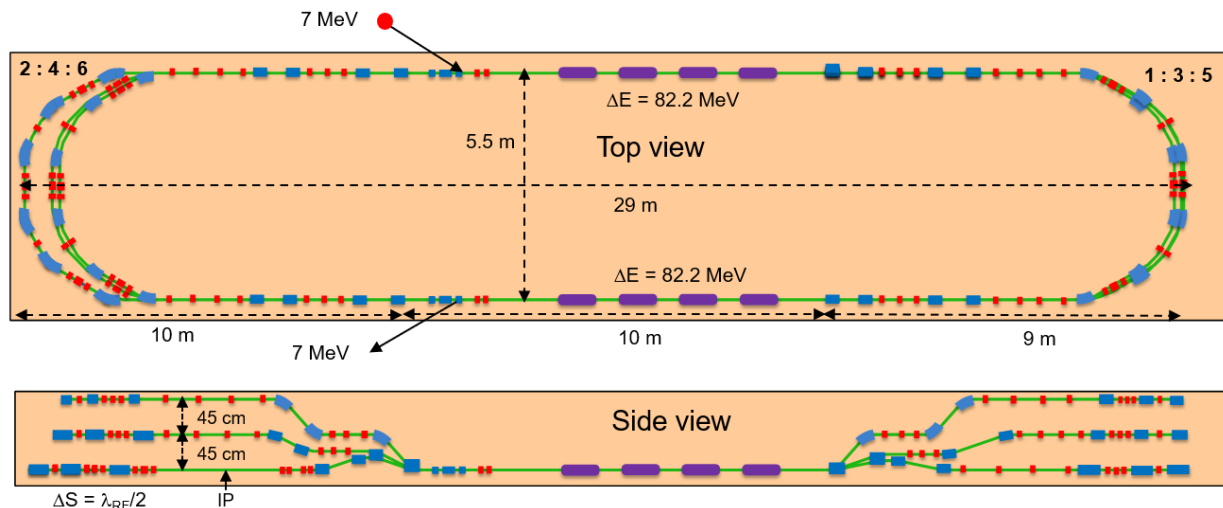


FIG. 1: Top and side views of PERLE, featuring two parallel linacs each hosting a 82.2 MeV cryomodule, achieving 500 MeV in three passes.

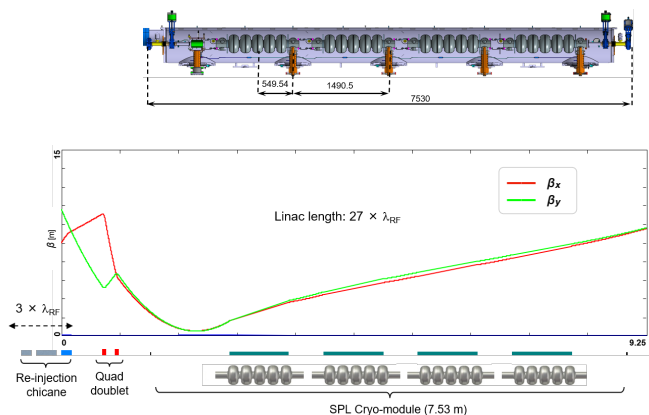


FIG. 2: Linac configured with the SPL cryomodule. The injection optics are tune-able by an initial quadrupole doublet (red).

The lower energy arcs (1, 2, 3) are composed of six 33 cm long curved  $30^\circ$  bends and of a series of quadrupoles (two triplets and one singlet), whilst the higher arcs (4, 5, 6) use double length 66 cm long curved bends. If rectangular bends were used their edge focusing would have caused a significant vertical focusing imbalance, which in turn would have adverse effect on the overall arc optics. Additionally the use of curved bends eliminates the problem of magnet sagitta, which would be especially significant for the longer 66 cm bends. Each arc is followed by a matching section and a mirror symmetric recombiner. As required in case of mirror symmetric linacs matching conditions described in the previous section impose mirror symmetric arc optics. Complete lattices for the lowest and highest energy arcs (arc 1 at 89 MeV and arc 6 at 500 MeV) comprising a spreader, 180 deg. horizontal arc and recombiner, are illustrated in Fig. 4. Presented

arc optics architecture features high degree of modular functionality to facilitate momentum compaction management, as well as orthogonal tune-ability for both the beta functions and dispersion. The path length of each arc is chosen to be an integer number of RF wavelengths, except for the highest energy pass whose length is longer by half of the RF wavelength to shift the RF phase from accelerating to decelerating. The optimal bunch recombination pattern gives some constraints on the length of the arcs, as described in Section V.

PERLE serving as a user facility is envisioned to host a number of experiments ranging from elastic ep scattering to laser-Compton back-scattering. For that purpose, the facility will accommodate a pair of 2.7 meter long experimental areas (IP) configured at top energy of 500 MeV. As illustrated in Fig. 4, the IPs are located symmetrically on both sides of arc 6. Their optics based on low-beta squeeze ( $\beta = 30$  cm) is configured with a triplet doublet pair. A second doublet completes the match to the horizontal 180 deg. arc.

### C. Staging the ERL construction

With minimal additional costs in hardware, it is feasible to split the construction of this machine into two phases: “250 MeV” version with one cryomodule and three straight sections at the opposite side [8] as shown in Fig. 5, and “500 MeV” version. The 250 MeV version of PERLE has a simpler structure with fewer elements, resulting in lower initial costs and faster construction and shorter commissioning time.

The fundamental difference of 250 MeV version is that the injection line and the dump are on the same side, that leads to a slightly longer common section (where bunches of different energies share the same beam pipe). However this version can host two low beta ( $\beta < 30$  cm) IRs at the

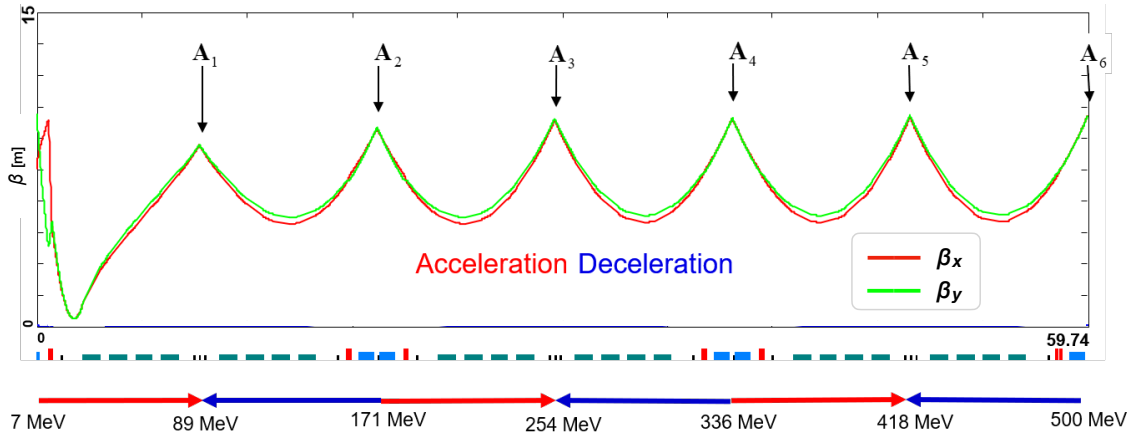


FIG. 3: Multi-pass linac optics. Red/Green curves illustrate symmetrically optimized horizontal/vertical beta functions across different passes through the linac; Red/Blue arrows indicate the accelerating/decelerating passes.

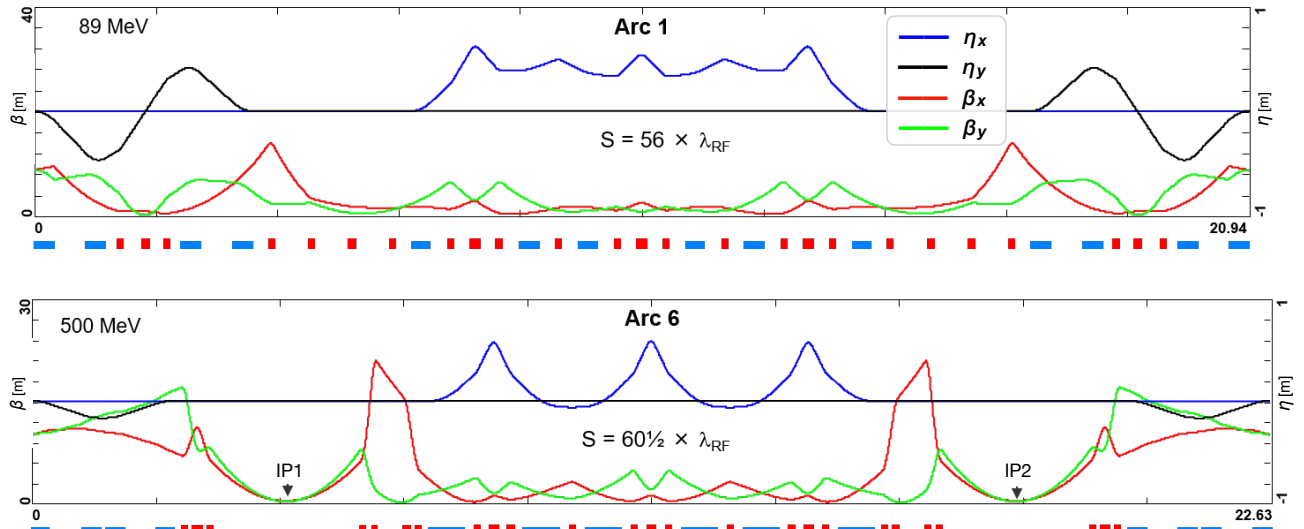


FIG. 4: The lowest and highest energy arcs (arc 1 and arc 6). Optics architecture based on the FMC cell. Horizontal (red curve) and vertical (green curve) beta-function amplitudes ( $\beta$ ) are illustrated. Blue and black curves represent the horizontal and vertical dispersion ( $\eta$ ) respectively. The arc as configured above is tuned to the isochronous condition.

highest energy straight section (see Fig. 6). This allows to keep the low footprint of the machine (under 30 meter long) and to have more space for the experiments. In the 500 MeV version, the highest energy arc section is extended in order to accommodate two experimental areas. The energy ratio at the arc sections of 250 MeV version is close to the one after the second cryomodule, thus, the corresponding switch-yard layouts are similar between the two versions.

In the 500 MeV version, the turning section utilizes the spreader-arc-recombiner to perform a 180-degree turn, guiding the beam towards the other linac. The 250 MeV version instead features a 'return loop' comprising spreader-arc-straight-arc-recombiner, executing a

complete 360° turn and directing the beam back to the same linac. The tune-ability of the arcs allows to keep the same arc in both versions with the same magnets closing the horizontal dispersion and momentum compaction bumps at the beginning of straight and common sections (Fig. 6).

### III. INJECTOR AND MERGER, SPACE CHARGE STUDIES

The PERLE injector will consist of a 350 kV high voltage DC photo-emission gun, a solenoid, a normal conducting 801.58 MHz buncher, a second solenoid, a

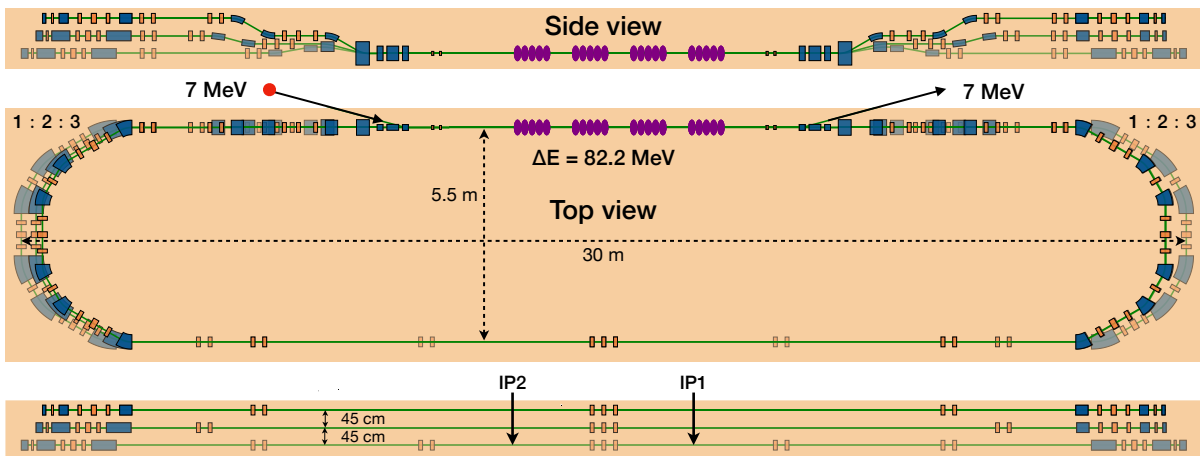


FIG. 5: Top and side views of 250 MeV version of PERLE, featuring one cryomodule on one side and three straight section on the opposite side, achieving about 250 MeV at the IPs.

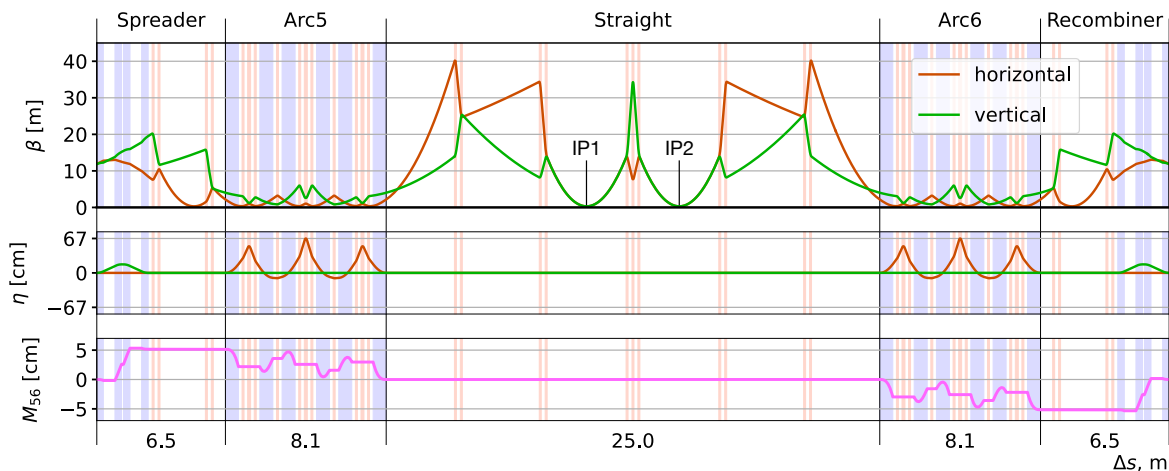


FIG. 6: The highest energy turn optics of the 250 MeV version of PERLE. Beta-function amplitude ( $\beta$ ) and dispersion ( $\eta$ ) are illustrated on the top and middle plots, respectively, in horizontal (red curves) and vertical (green curves) planes. Momentum compaction factor ( $M_{56}$ ) is presented on the bottom plot. Dipole and quadrupole magnets are the blue and orange areas.

four cavity superconducting 801.58 MHz main harmonic booster and a three dipole merger, as shown in Fig. 7. The injector must provide 500 pC bunches at a repetition rate of 40.1 MHz, accelerate them to the injection energy of 7 MeV, perform the initial longitudinal compression and optics matching the ERL loop while minimizing emittance growth.

#### A. Photo-cathode gun design and optimisation

The bunches are produced and initially accelerated in a 350 kV DC photo-emission gun. It will use an alkali antimonide photo-cathode illuminated with a 532 nm wavelength laser pulses. An alkali antimonide photo-cathode

has been chosen over other options such as gallium arsenide due to its less demanding vacuum requirements and ability to deliver beams with 20 mA average current using commercially available lasers. Design of the electrode system of the gun and temporal and spatial parameters of the laser pulse are optimised to deliver bunches with minimal transverse emittance.

#### B. Transverse dynamics and emittance preservation

The transverse focusing needs to be optimized such that the beam is small enough to fit through all apertures, so that it is matched to the ERL loop, and to preserve the transverse emittance. The evolution of this optimized

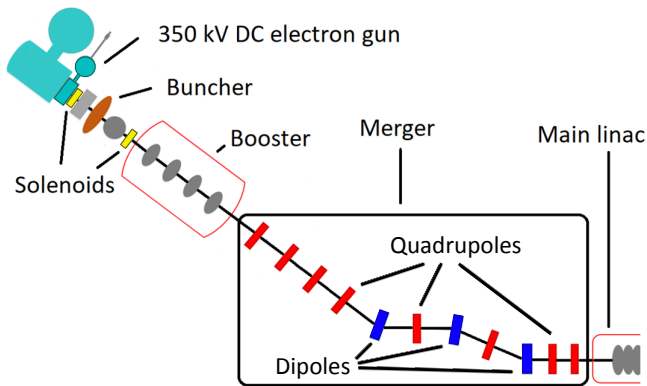


FIG. 7: The layout of the PERLE injector from the electron gun to the injection into the main linac with the components labeled.

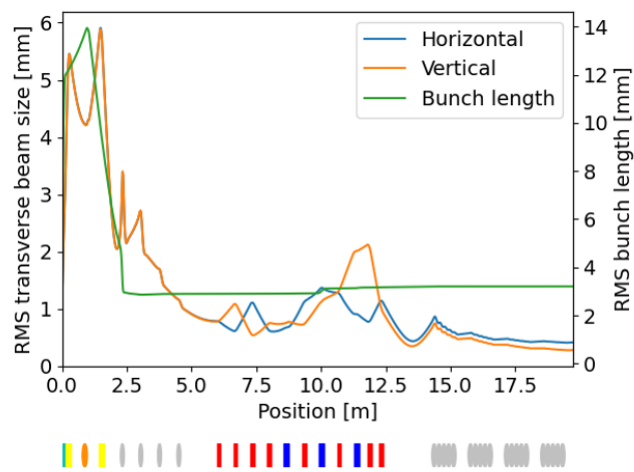


FIG. 8: The evolution of the RMS beam sizes along the injector. The location of elements is marked below the plot. The electron gun is marked in cyan, solenoids in yellow, normal conducting RF cavities in orange, SRF cavities in grey, quadrupoles in red and dipoles in blue.

transverse beam size can be seen in Fig. 8. The lower bound on the achievable emittance is set by the initial emittance produced at the cathode. This depends on the transverse laser spot size, the cathode material and the photo-injector laser wavelength. A smaller laser spot produces a lower emittance, however the space charge field sets a limit on the amount of charge that can be extracted at a particular spot size.

The evolution of the transverse emittance through the injector following the cathode can be seen in Fig. 9. Linear space charge can cause emittance mismatch to the design lattice, this can be mitigated by a technique known as *emittance compensation* [9]. As the 500 pC, 7 MeV beam still experiences significant space charge forces the emittance can still grow within the merger. The breaking of axial symmetry by the dipoles and quadrupoles of

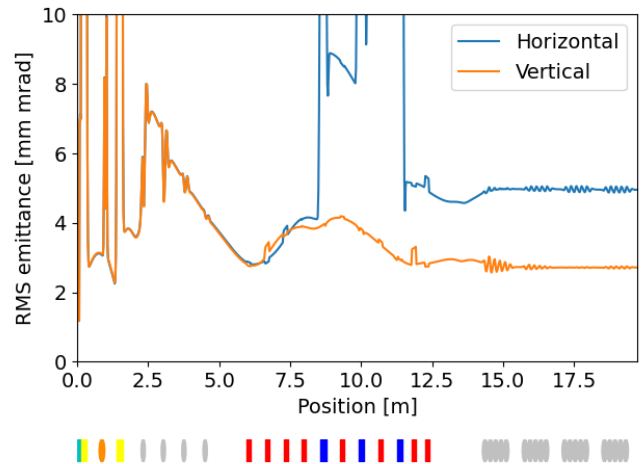


FIG. 9: The evolution of the RMS transverse emittance along the injector. The location of elements is marked below the below the plot. The electron gun is marked in cyan, solenoids in yellow, normal conducting RF cavities in orange, SRF cavities in grey, quadrupoles in red and dipoles in blue.

the merger complicates this emittance compensation. In the case of the PERLE injector, simultaneous emittance compensation in both planes cannot be achieved.

Non-linear space charge can also cause growth in the emittance. This affects the slice emittance in addition to the projected emittance. Geometric and chromatic aberrations also contribute to the total emittance growth. In the merger horizontal bending plane there is an additional space charge related emittance growth mechanism. The longitudinal space charge forces of the bunch cause the particles at the front and back to change energy as they move through the merger. Therefore they are bent differently by the dipoles, forming induced residual dispersion at the exit of the merger and hence emittance growth [10]. The final achieved normalised emittances are 5.0 mm·mrad in the horizontal plane and 2.7 mm·mrad in the vertical plane. These are both within the specification of less than 6 mm·mrad.

### C. Acceleration, bunch compression and longitudinal phase space linearity

The booster linac accelerates the beam from 350 keV, the energy that it leaves the electron gun, up to the injection energy of 7 MeV. It consists of four single cell SRF cavities with individually controllable amplitudes and phases. In addition to accelerating it is also used for longitudinal phase space manipulations during the bunching process as discussed below.

The initial longitudinal bunch compression in PERLE is performed in the injector and can be seen in Fig. 8. Initially a long bunch is created at the cathode to mini-

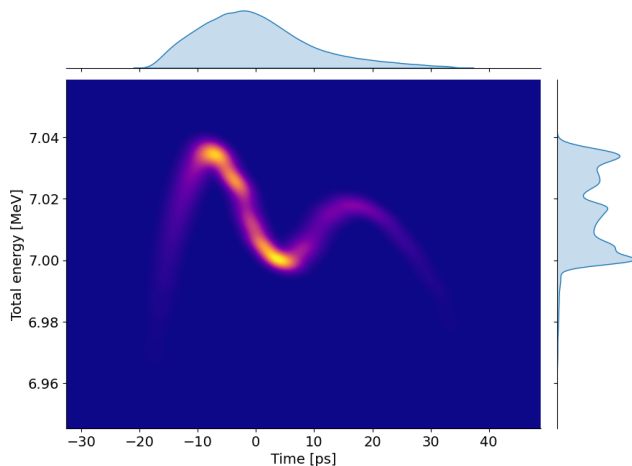


FIG. 10: The longitudinal phase space after the merger and before the main linac with projected particle position (horizontal) and energy (vertical) distributions.

mize the space charge forces and the resulting emittance growth. This bunch then elongates after the gun due to its space charge forces and is then compressed mainly by using the normal conducting buncher cavity, but additionally there is some velocity bunching in the first cavity of the booster linac. The merger has a non-zero M56 and could be used to perform further bunch compression but that approach is not used in this configuration. Instead the last cell of the booster is used to dechirp the beam, minimising the energy spread through the merger.

Maintaining a linear longitudinal phase space with small longitudinal emittance at the exit of the injector is also important so that minimum energy spread can be obtained at the IP. The longitudinal phase space just before entering the main linac can be seen in Fig. 10. There is some non-linearity in this phase space, resembling an "M" shape. This shape emerges from the interplay of the non-linearity of the ballistic bunching process, space charge and the booster linac RF curvature. The ballistic bunching in the drift between the buncher and booster is non-linear causing the longitudinal charge distribution to become asymmetric with more charge at the front and a lower charge tail. Additionally, during this the space charge is accelerating the front of the bunch and decelerating the back, causing the bunch to dechirp. As the charge distribution is asymmetric, the space charge forces at the front of the bunch are stronger so the front gains energy faster than the back. This leads to the formation of a "V" shaped longitudinal phase space just prior to the entrance to the booster. The RF curvature of the booster then imposes a second-order distortion to the longitudinal phase space producing the outer wings of the "M" shape. The asymmetry in the height of the "M" distribution then forms in the merger due to the stronger space charge at the front of the bunch. The addition of higher harmonic cavities to the injector (either a normal conducting cavity before the buncher cavity or an SRF

cavity in the booster) could help with symmetrizing the charge distribution and linearizing the longitudinal phase space [11].

#### D. Status of the electron injector design and possible improvements

The PERLE injector meets the specification achieving transverse normalized emittance of less than 6 mm-mrad and compressing the bunch to the required length. Further improvements could potentially be obtained by transverse shaping of the laser pulse on the cathode to reduce the non-linear space charge forces. For example a one sigma cut of the initial Gaussian distribution could be used to produce bunches with more linear space charge [12]. Reducing the horizontal emittance growth in the merger would also be of benefit. This could be achieved by matching the optics into the merger so that the transverse phase space has the correct orientation to minimize the transverse emittance growth due to the longitudinal space charge induced residual dispersion [10]. Our initial goal was to 'split' values of the horizontal and vertical betas (make them vastly different as favored by the upstream injection chicane optics. Certainly, another doublet could be added to facilitate full tunability of both betas and alphas. This is presently being considered to provide flexibility to match into the merger and then to match the parameters required at the entrance of the main linac.

## IV. LONGITUDINAL MATCH

### A. On crest match

To first order the desired longitudinal match can be obtained by keeping all arcs isochronous with path-lengths of a multiple of RF wavelengths and initial linac phases on crest. This configuration results in a longitudinal phase space at the interaction regions where the final energy spread is dominated by the effect of the RF curvature imprinted on the bunch.

In order to minimize energy spread at the interaction region, for this configuration, one would need to assure sufficient longitudinal phase space available for the injected bunch. This would mitigate the effect a pronounced longitudinal curvature, resulting in a large energy spread. Additionally, as the bunch reaches the dump, this energy spread is replicated with the added distortion from the arc longitudinal dispersion. We therefore move off-crest within the ERL loop from pass-to-pass and utilise every arcs FMC lattice to tailor the first and second order momentum compaction at each pass, resulting in a minimized energy spread at the IP, injection and dump simultaneously.

## B. Energy spread minimization

We denote for linacs 1 and 2 the first accelerating RF phases of  $\phi_{1,1}$  and  $\phi_{2,1}$  respectively, and we denote for arc 1 through 6 path length deviations from an integer number of RF wavelengths  $\Delta\phi_i$  with  $i$  indicating the corresponding arc. Successive RF phases correspond to the previous phase plus the offset obtained by the following two arcs. In this way for example  $\phi_{1,2} = \phi_{1,1} + \Delta\phi_1\Delta\phi_2$  and  $\phi_{2,2} = \phi_{2,1} + \Delta\phi_2\Delta\phi_3$ .

Following the semi-analytic method of [13] with respect to energy spread minimizing matches in a common transport ERL, we choose the RF phase configuration shown in Fig. 11 which can be obtained by modifying the path lengths of arcs 1, 4 and 6 by  $-30$ ,  $+30$  and  $-30$  degrees respectively.

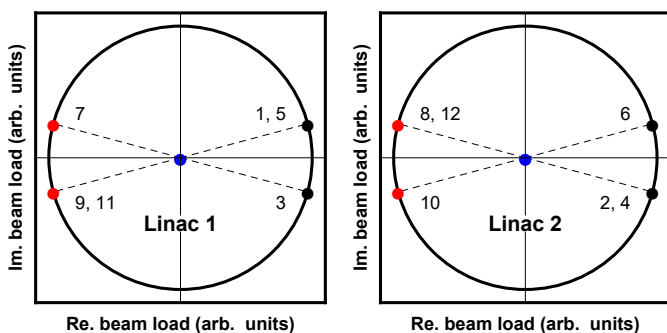


FIG. 11: rf beam load diagram of linacs 1 and 2 with phase choices during acceleration (black), deceleration (red), and resultant RF load (blue).

With this set of phases, during acceleration the beam traversing through arc 1 has a chirp of opposite sign to when it reaches arc 4. During deceleration, these signs change. In this manner, the lengthening and shortening of the bunch tails as the bunch is linearized will compensate, resulting in a bunch with a controlled bunch length.

Due to the symmetry of the system, a set of  $T_{566}$  values for the arcs that linearizes the bunch at the top energy also returns the bunch to its initial curvature as it reaches the dump. Therefore, the objective of linearizing the bunch towards the IP tuning two arcs is an under-constrained problem. A study of the possible configurations is shown in Fig. 12, where by setting one of the arcs  $T_{566}$  values and solving for the other, the longitudinal phase spaces at the IP and dump are compared for the effectiveness of the bunch length control scheme. Additionally, the change between the initial and final  $T_{566}$  value of the arcs must also be taken into account as greater changes will require stronger corrections with correspondingly stronger sextupole fields.

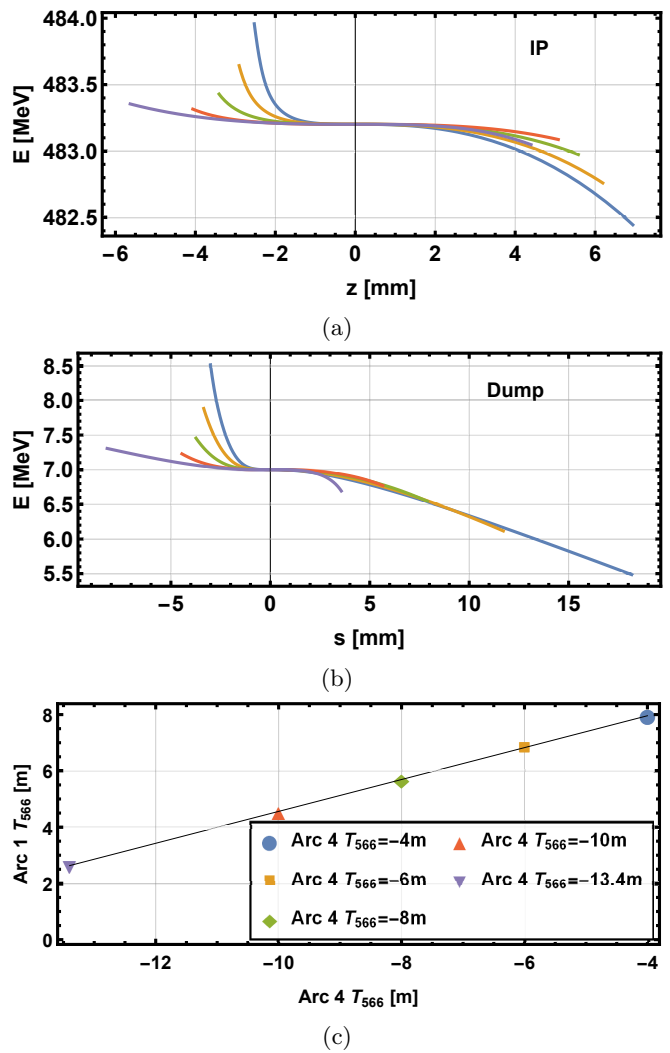


FIG. 12: Longitudinal phase spaces at (a) the interaction region and (b) dump for (c) different combinations of linearizing  $T_{566}$  in arcs 1 and 4, with line indicating a continuous set of solutions available.

## C. Partial compression

A modest compression of the bunch in the first arc by deviating from the isochronous condition, would reduce the degrees of RF that the bunch sees for the rest of the accelerating passes and hence reduce the curvature to be corrected tuning the arc  $T_{566}$  values. In order to compensate the change in the bunch chirp during the compression, the linac phases must shift accordingly. This can be treated as a perturbation from our previous solution for small compression where the magnitude of the off-crest angle of the first accelerating pass is decreased. The corresponding change in path lengths also affects the phase of the last decelerating pass going equally further off-trough. This strategy is eventually limited by the range of  $R_{56}$  values available from the arc FMC lattice. An example set of phases is shown in Fig. 13. Again, the

symmetry of the system is such that during deceleration, the compressed bunch reaches arc 1 with the opposite sign of chirp and is decompressed such that during the last deceleration towards the dump the beam chirp is cancelled, as shown in Fig. 14. Here, the modified arc parameters are for arc 1:  $R_{56} = 0.05$  m,  $T_{566} = 6.49$  m and arc 4  $T_{566} = -10$  m.

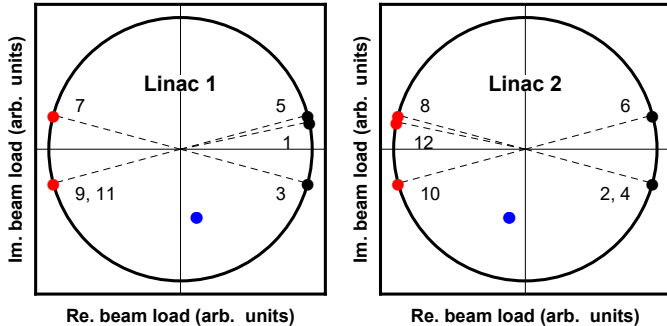


FIG. 13: RF beam load plots for linacs 1 and 2 for a longitudinal match with a non-isochronous arc 1 showing phase choices during acceleration (black), deceleration (red), and 10 times the resultant (blue)

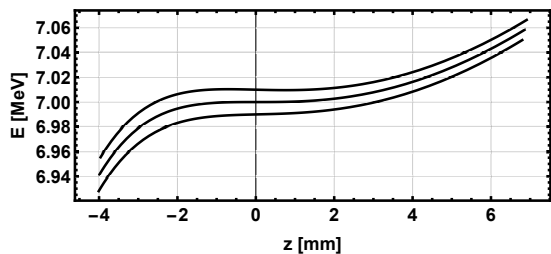


FIG. 14: Longitudinal phase space towards the dump.

## V. CONSIDERATIONS OF FILLING PATTERN AND BUNCH TIMING OPTIONS

PERLE is proposed to consist of 6 circulations, 3 up-pass and 3 down-passes. There are a total of  $(N - 1)! = 120$  unique filling patterns, where  $N$  is the total number of circulations. If there were no restrictions on how the filling pattern on one turn evolves on subsequent turns, there would be a grand total of 1728 possible combinations of filling pattern and recirculation scheme to consider. However, due to considerations relating to collective effects and simplicity of the injection timing, we choose to impose the following constraints on the filling patterns and recirculation scheme:

- The filling pattern each turn must be the same
- The bunch spacings must be as uniform as possible

The first constraint implies adoption of a sequence preserving (SP) recirculation scheme [14, 15]. An SP scheme

TABLE II: Allowed filling patterns of PERLE.

|               |               |               |               |
|---------------|---------------|---------------|---------------|
| [1 3 5 2 4 6] | [1 3 5 2 6 4] | [1 3 5 4 2 6] | [1 3 5 4 6 2] |
| [1 3 5 6 2 4] | [1 3 5 6 4 2] | [1 5 3 2 4 6] | [1 5 3 2 6 4] |
| [1 5 3 4 2 6] | [1 5 3 4 6 2] | [1 5 3 6 2 4] | [1 5 3 6 4 2] |

is one whereby the bunch on its first turn moves to the bucket previously occupied by the bunch on its second turn, 2 moves to 3 and so on. In this scheme, the bucket previously occupied by the bunch on its first turn is always available to inject the new bunch into and the RF transients in the RF cavities is the same every turn. This has the benefit of simplifying the injection timing, which can only be regular for SP schemes. The other point to note is that all filling patterns have an associated SP scheme.

The second constraint implies that the bunches must alternate between accelerating and decelerating, to keep the bunch spacing as regular as possible.

We define the filling pattern as an  $N$ -dimensional row vector, where the index is the turn number and the value is the bucket number. We can then define a transition set, which is another  $N$ -dimensional row vector enumerating how many buckets each bunch shifts on a single turn. While this convention is less intuitive than defining the vector index as the bucket number, it has the benefit that we can define the filling pattern on the next turn by simply adding the current filling pattern to the transition set. However, we must remember that after each turn, the bunch previously on its first turn is now on its second, second is now on its third and so forth. To write this formally:

$$\begin{aligned} \mathbf{F}^{(n)} + \mathbf{T}^{(n)} &= C_{-1}(\mathbf{F}^{(n+1)}) \\ \mathbf{T}^{(n+1)} &= C_1(\mathbf{T}^{(n)}) \end{aligned} \quad (1)$$

where  $\mathbf{F}^{(n)}$  and  $\mathbf{T}^{(n)}$  represent the filling pattern and transition set respectively on turn  $n$ , and  $C_n$  is a cyclic permutation to the left by  $n$  places, so  $C_1([1 2 3 4 5 6]) = [2 3 4 5 6 1]$  and are represented as vectors. Based on our two constraints there are a total of 12 possible filling patterns, and from the earlier discussion, each will have a unique SP transition set associated to it. Table II shows the allowed filling patterns for PERLE.

While the number of possible machine configurations to consider is greatly reduced, there are other factors to consider, which adds further complexity to the filling pattern analysis for PERLE. The key issue being that PERLE is designed to have a harmonic number of 20, which means that each bunch train comprising of 6 bunches, each on a different turn number, must occupy a total of 20 RF cycles. However, 20 is not divisible by 3, and therefore five of the bunch spacings must be 3.5 RF cycles and the other must be 2.5 RF cycles, the choice between which of the bunches the 2.5 RF cycle spacing goes is an additional degree of freedom.

The choice of filling pattern, bunch spacing pattern and recirculation scheme, which we shall refer to more generally as the bunch train structure, directly affects the transients experienced in the RF cavities, in turn affecting the stability and performance of the RF system, the beam stability and the RF power requirements. However, as discussed in [14], an SP scheme with alternating accelerating and decelerating bunches is the global optimum for RF and beam stability as subsequent bunches cancel the transients induced by the previous bunch. All the allowed filling patterns in PERLE are of this form, therefore the beam and RF stability is inherently optimised regarding the fundamental operating mode of the cavity.

The bunch train structure also directly affects the beam break-up instability (BBU) experienced by the machine, and can have a considerable impact on the beam threshold current. Reference [15] explores the impact on threshold current from different bunch train structures. This is a consideration which will be explored in future detail in future. BBU is an inherently nonlinear effect, sensitive to factors such as HOM frequency and bunch spacing and filling pattern. The effect of bunch train structure on the threshold current is difficult to explore analytically and requires comprehensive simulation studies to explore the effect of varying different parameters. This analysis should be repeated for any changes in beam line or cavity design.

A third factor which is affected by the choice of bunch train structure are the lengths of each arc in the ERL ring. The transition set determines how many RF buckets a bunch moves on a given turn, implying that the circumference of each turn is different for each filling pattern. It is possible to consider bunch train structures with a certain difference in arc lengths on one side in order to provide space for an insertion device. In order to look at how the length of the machine relates to the filling pattern, it is convenient to consider filling patterns with respect to RF cycle rather than RF buckets. To do so, we simply need to replace the RF bucket number with the RF cycle number. For example, in the case where the 2.5 cycle spacing is between the first two bunches, the timings of each bunch, regardless of which turn number they are on would become [0 2.5 6 9.5 13 16.5], and so filling pattern [135246] becomes [0 6 13 2.5 9.5 16.5], where the values correspond to the RF cycle number and the index remains the turn number.

From Eq. 1, by re-indexing and the fact that a cyclic permutation is a linear operation, we can write:

$$\begin{aligned} F_2 - F_1 &= T_1 \\ F_3 - F_2 &= T_2 \\ \dots & \\ F_6 - F_5 &= T_5 \\ F_1 - F_6 &= T_6 \end{aligned} \quad (2)$$

We can always define  $F_1 = 1$  as we are simply defining which RF cycle we consider the "first" cycle on a given

turn number; whereby  $F_i$  and  $T_i$  are the  $i^{\text{th}}$  element of the filling pattern and transition set vectors respectively on a given turn. We can also write the transition set in terms of the length of the straight sections,  $L$ , and the arc lengths traversed on that turn  $A_n$ . For the time delay between extraction of the bunch on turn 6 and the injection of a new bunch, we define this as  $A_0$  and consider it as a fictitious arc length. Now Eq. 2 becomes:

$$\begin{aligned} F_2 - F_1 &= 2L + A_1 + A_2 \\ F_3 - F_2 &= 2L + A_3 + A_4 \\ F_4 - F_3 &= 2L + A_5 + A_6 \\ F_5 - F_4 &= 2L + A_5 + A_4 \\ F_6 - F_5 &= 2L + A_3 + A_2 \\ F_1 - F_6 &= 2L + A_1 + A_0 \end{aligned} \quad (3)$$

From this equation, the filling pattern elements are known for a specific bunch train structure, therefore the arc lengths can be considered as unknowns. There are 7 unknowns ( $A_0 - A_6$ ) and 6 equations, but we can choose to constrain one of the arc lengths (in this example,  $A_6$ ), and solve to obtain:

$$\begin{aligned} A_0 &= (A_6 - 2F_4) + F_1 + F_1 \\ A_2 &= (A_6 - 2F_4) + F_2 + F_6 \\ A_4 &= (A_6 - 2F_4) + F_3 + F_5 \\ A_1 &= -(2L + (A_6 - 2F_4)) - F_1 - F_6 \\ A_3 &= -(2L + (A_6 - 2F_4)) - F_2 - F_5 \\ A_5 &= -(2L + (A_6 - 2F_4)) - F_3 - F_4 \end{aligned} \quad (4)$$

The odd numbered arcs are on the right side as viewed on the diagram shown in Fig. 1, and the even numbered arcs are on the left. From Eq. 4, we can see that the lengths of the even arcs are directly proportional to the length of Arc 6. By increasing the length of Arc 6, the odd arcs decrease in length and the even arcs increase. In order to change the difference in arc lengths on one side, we would need to change the bunch train structure.

## VI. START-TO-END PLACET SIMULATION WITH CSR AND WAKES

### A. Coherent Synchrotron Radiation in the ERL

There is a negligible effect of the incoherent synchrotron radiation in terms of geometric emittance growth and energy loss due to the low energy of the beam. However, due to the large bunch intensity, the Coherent Synchrotron Radiation (CSR) distorts the beam longitudinally, which through dispersion affects the transverse plane leading to potential losses. Longer bunches are less affected by CSR, but do experience the non linearity of the RF field [16]. Thus, an intermediate bunch length has been studied in order to observe the effect of the CSR, including an increase of the beam current, without

having a combination with the strong curvature due to the RF electric field. The impact of CSR is shown in Fig. 15. A beam current of 10 mA only slightly modifies the longitudinal phase space distribution, whereas a micro-bunching phenomenon appears for 30 mA although it does so without causing particle losses. The injec-

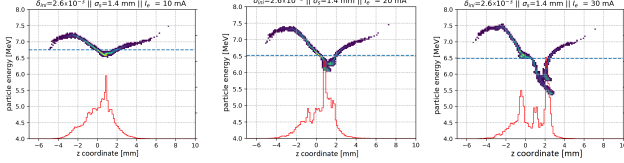


FIG. 15: Longitudinal phase space at the dump including CSR for different beam current and a longitudinal emittance of 25 keV mm. The histogram in red represents the longitudinal distribution. **Left:** Results with 10 mA. **Center:** Results with 20 mA **Right:** Results with 30 mA.

tion longitudinal emittance has been modified in order to observe the influence of the CSR on the longitudinal distribution at the dump. As the energy deviation increases, the effects of the CSR tends to be hidden within a wider energy distribution as shown in Fig. 16. From what we have observed, the main effect of CSR should occur at lowest energies (merger and dump at 7 MeV and a bit less in arcs at 89 MeV). A back-of-an-envelope calculation suggests a wavelength of around 0.25 mm for the synchrotron radiation emitted in dipoles at 7 MeV, which would explain why the effect is so "coherent" and why it is pronounced for bunch lengths of 0.5 mm. The wavelength of synchrotron radiation at higher energies is even lower, so it should be less coherent.'

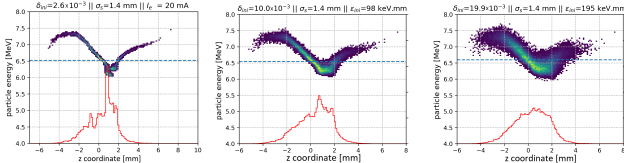


FIG. 16: Longitudinal phase space at the dump including CSR for 20 mA beam current and different injection longitudinal emittance. The histogram in red represents the longitudinal distribution. **Left:** Results with 25 keV mm. **Center:** Results with 98 keV mm. **Right:** Results with 195 keV mm.

The PLACET tracking results give full transmission for a bunch length of 1.4 mm. However, a transmission of 99.5% is obtained with a 3.0 mm bunch length due to the large distortion created by the curvature of the RF electric field as the beam is accelerated on-crest. Furthermore, the CSR shows an increasing impact on the longitudinal phase space as the bunch charge increases. The micro-bunching that appears at a beam current close to 30 mA does not lead to losses for a bunch length of

1.4 mm. Finally, the coherent synchrotron radiation features a wavelength in the order of the bunch length that is the same order of magnitude as the beam pipe. A beam pipe of 40 mm × 90 mm (H/V) is foreseen in the dipoles and is expected to be effective at mitigating part of the CSR. Further shielding studies with CSR impedance should follow.

Therefore, an appropriate choice of the beam pipe dimensions and coating should be sufficient to mitigate CSR in the PERLE accelerator.

These longitudinal phase space distortions, obtained with PLACET2[17], have been reproduced in the same conditions with BMAD[18] and show a great consistency between the two codes. Fig. 17, obtained with BMAD, shows the effect of the bunch length on the longitudinal phase space of the beam, where shorter bunches are dominated by CSR and longer bunches are dominated by the RF non-linearity.

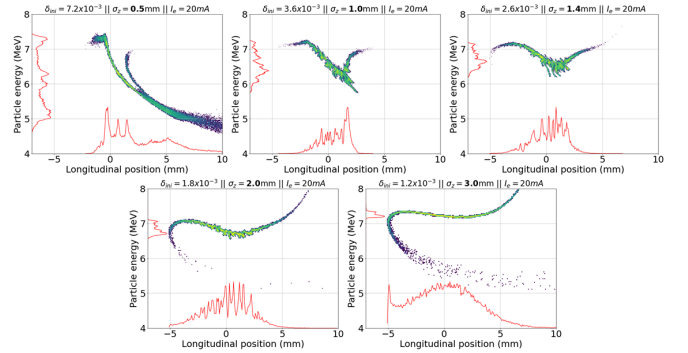


FIG. 17: BMAD simulations showing longitudinal phase space at the dump including CSR for 20 mA beam current and different bunch length. The histograms in red represents the longitudinal and energy distributions. **Top left:** Results with 0.5 mm. **Top center:** Results with 1.0 mm. **Top right:** Results with 1.4 mm. **Bottom left:** Results with 2.0 mm. **Bottom right:** Results with 3.0 mm.

Bunching effects were investigated in the arcs. However, the cumulative effect was presented at the dump to compare the RF and CSR contributions. Simulation results illustrated in Fig. 15 and Fig. 17 can be interpreted as density modulations.

## B. Multi-bunch tracking of the ERL

After successful lossless single bunch tracking including CSR, multi-bunch tracking was studied with the addition of the long range wake-field interaction between bunches. The HOM are those of the SPL cavity scaled to 801.58 MHz and with a single quality factor of  $10^5$  for all the modes, that is the highest quality factor among the modes of the SPL cavity, following the assumptions as in [5]. We observe the amplitude of the 52 horizontal and vertical modes over time with each bunch passage

in the RF cavities. 5000 macro-particles are sent every 25 ns in order to reproduce the operation of the ERL at nominal beam current and beyond. The objective is to observe if at least one of the high order mode is excited and sees its amplitude increasing, which is symptomatic of potential beam instabilities during a long term operation.

### 1. Beam current threshold

The multi-bunch tracking results show that there is no increase of any mode amplitudes with a bunch charge of 500 pC or 20 mA beam current over the time period studied as shown in Fig. 18 (left). However, a threshold is attained for a beam current of 200 mA for which the amplitude of one mode builds up. Eventually, this mode may excite other modes and lead to instabilities in long term operation. This threshold is far from the design beam current, however particle tracking studies are based on a 250 ms time period and may overestimate the threshold. Nonetheless, a convincing amplitude increase of one of the modes needs to be observed to conclude in a threshold being attained. Even if the threshold may

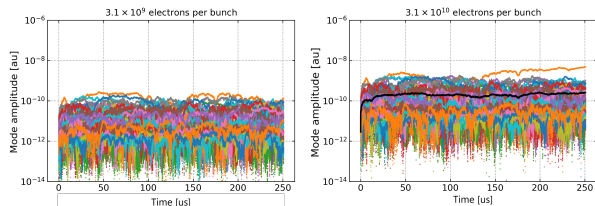


FIG. 18: Study of the HOM amplitudes as a function of the time. A new electron bunch is injected every 25 ns. **Left:** A beam current of 20 mA. **Right:** A beam current of 200 mA.

be overestimated, a factor 10 with respect to the design beam current is a substantial margin. Some solutions are presented in the next sections to increase further the threshold and provide further margin.

### 2. Recombination pattern influence

The bunch recombination pattern in the linacs has an influence on the beam current threshold. The best bunch recombination patterns ensure both the alternation of accelerating and decelerating bunches as well as the maximal distance between the newly injected bunches and the bunches heading to the dump. The current ERL design does not provide this last condition as shown in Fig. 19. The extension of the return arc 6 by  $12\lambda_{RF}$  brings the bunch recombination pattern from a  $7-7-10.5\lambda_{RF}$  turn-by-turn path-length adjustment that only alternates accelerating and decelerating bunches to a  $7-7-2.5\lambda_{RF}$  turn-by-turn path-length adjustment

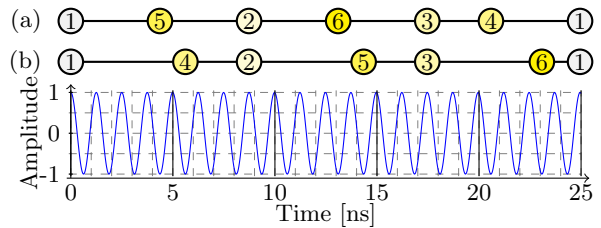


FIG. 19: Bunch recombination pattern optimising the distance between the newly injected bunch 1 and the bunch 6 going to the dump (a) and the pattern obtained from the unoptimised arc turn-by-turn path-length (b). The cavity voltage is presented as a function of the time. The bunch 1 represents the injection of a new bunch every 25 ns. The bunches 2,3,4,5,6 represent the position of the bunch after 1,2,3,4,5 turns respectively. There is an alternation of accelerating and decelerating bunches.

that verifies both conditions. The two bunch recombination patterns shown in Fig. 19 have their simulation results compared and presented in Fig. 20. The slope with

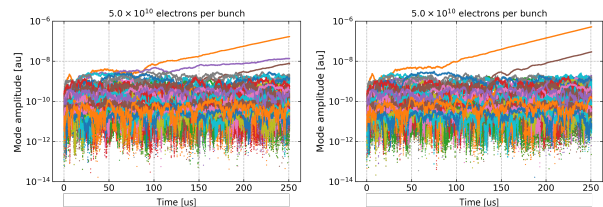


FIG. 20: Study of the HOM amplitudes as a function of the time. A new electron bunch is injected every 25 ns. **Left:** The arc lattice without the optimised bunch recombination pattern. **Right:** Optimised bunch recombination pattern.

which the mode amplitude increases is reduced with the optimised bunch recombination pattern. It proves the beneficial influence of the optimised pattern and confirms that the bunch recombination pattern can decrease the strength of the long range wake-fields interaction in the RF cavities. Therefore, the ERL lattice needs to be carefully fine tuned in order to achieve one of the best bunch recombination pattern and ensure margin with the design beam current and a long term stability of the machine.

## VII. BEAM BREAKUP STUDIES

Bunches passing through the cavity inherently have finite offsets, these may excite Higher Order Modes (HOMs). Mono-pole modes add/subtract energy from the beam, causing energy and timing jitters, which can lead to longitudinal beam breakup (BBU). However in ERLs, transverse BBU is dominant, here the transverse offset of a bunch creates dipole HOMs, which kick subse-

quent bunches. Due to recirculation, this forms a positive feedback loop that causes the beam offset and HOM voltage to grow. This is known as regenerative beam breakup instability and it sets the beam threshold current for stable beam operation in an ERL [19, 20].

Recent studies have shown that the choice of filling pattern and recirculation scheme for a multi-pass ERL can drastically affect the interactions between the beam with the RF system and BBU instabilities [14, 15]. A factor of 6 difference between the best and worst pattern in threshold current was observed in simulations. In this work, we investigated BBU instability of PERLE with simulation by building an 8-cavity BBU tracking model with filling pattern dependence and compared it to an analytical model.

### A. 8-cavity BBU tracking model

As the concept of filling patterns for ERLs is relatively new, none of the existing BBU simulation codes incorporated it in their calculations. Therefore, we have adapted the ERLBBU algorithm [20–22] and developed a new simulation tool to simulate BBU with filling pattern dependence. The previous version of the code had only a single cavity [15]. As the PERLE design has 8 cavities, we developed a new 8-cavity BBU tracking model.

In this model, the HOM voltages of the 8 cavities are tracked as shown in Fig. 21 (a) as particles pass through the cavities. The different colors represent HOM voltages at different loaded Q-factors,  $Q_L$ . The injection current of PERLE is 20 mA. In a 6-pass ERL like PERLE, each bunch passes through the cavity 6 times, hence the actual current seen by the cavities is 6 times the injection, i.e. operation current  $I_{op} = 120$  mA. The HOM here is TE111  $4\pi/5$  mode with 1.0365 GHz frequency, which is one of the dominant modes. We can see the  $Q_L$  has to be  $\leq 1.7 \times 10^5$  to prevent the HOM voltage growing. This indicates the  $Q_L = 1.7 \times 10^5$  is the critical  $Q_L$  for this mode. To operate PERLE at 20 mA injection current, the  $Q_L$  of TE111  $4\pi/5$  mode must be damped below this critical  $Q_L$ .

The bunches are tracked through transfer matrices of PERLE, which were extracted from the OptiMX model. The code tracks macro particles rather than single particles. Each macro particle represents a single bunch, carries the charge of one bunch and its position represents the bunch centroid. Injected initial bunches are transported to the 1<sup>st</sup> cavity by the transfer matrix between injection point and 1<sup>st</sup>, then the excited HOM voltage  $\delta V_H$  is calculated by

$$\delta V_H = \frac{\omega_H^2}{2c} q_b \left( \frac{R}{Q} \right)_H x \quad (5)$$

where  $\omega_H = 2\pi f_H$  with  $f_H$  being the HOM frequency,  $q_b$  is the bunch charge,  $\left( \frac{R}{Q} \right)_H$  is geometric shunt impedance

of the HOM, and  $x$  is the bunch offset. To speed up the simulation time, the initial HOM voltage is set to be 1 or 10 kV. Then  $\delta V_H$  is added to the existing HOM voltage  $V_H = V_H + \delta V_H$ . The voltage when the next bunch arrives  $dt$  is

$$V_H(dt) = V_H e^{-\frac{\omega_H dt}{2Q_L}} e^{i\omega_H dt} \quad (6)$$

where  $Q_L$  is loaded HOM Q-factor. The next bunch will receive a kick  $\Delta x'$  from the HOM given as

$$\Delta x' = \frac{V_{H, I}}{V_{beam}} \quad (7)$$

where  $V_{H, I}$  is the imaginary part of the HOM voltage (as the kick is from the magnetic field) and  $V_{beam}$  is the beam voltage,  $pc/e$ . Then bunches are transported to the next cavity by transfer matrix between the current cavity and the next cavity and the process is repeated. After 8 cavities and 6 turns, the bunches are dumped and replaced by newly injected bunches. The standard deviation of the bunch centroid  $\sigma_x$  at cavities are shown in Fig. 21 (b). The blue, red, and green lines correspond to when the  $Q_L$  is below, at, and above the critical  $Q_L$  value. The black line is the RMS beam size estimated in the OptiMX (of course, without BBU instability). We can see when the HOM voltage is higher, the  $\sigma_x$  is larger, which indicates bunches received more kicks.

### B. Simulation results

We estimated critical  $Q_L$ s for the first 15 dominant HOM modes and the results are shown in Fig. 22. The injection current is 20 mA. The results are compared to the analytical model in Ref. [23, 24], which estimates threshold current of a single mode as

$$I_{th} = - \frac{2E}{e(R/Q)_\lambda Q_\lambda k_\lambda \sum_{j>i=1}^{N_c} (E/E_j) M_{12}^{ij} \sin(\omega_\lambda t_r^{ij})}, \quad (8)$$

where  $E$  is the energy of the beam in the recirculation arc,  $E_j$  is the beam energy at checkpoint  $j$ ,  $M_{12}^{ij}$  is a matrix element of  $M^{ij}$ , which is the transfer matrix from the  $i^{th}$  checkpoint to the  $j^{th}$  checkpoint, and  $t_r^{ij}$  is the corresponding transit time. Here  $N_c$  is the number of considered checkpoints, which are located at exits of linacs. Here threshold current is calculated for the horizontal modes and for vertical modes the  $M_{12}$  is replaced by  $M_{34}$ .  $\lambda$  denotes the dipole mode number,  $k_\lambda$  is wave number,  $(R/Q)_\lambda$  is shunt impedance,  $Q_\lambda$  is quality factor,  $e$  is electron charge. In this context, the threshold current is calculated for the horizontal modes, while for vertical modes,  $M_{12}^{ij}$  is substituted with  $M_{34}^{ij}$ . Here,  $\lambda$  represents the dipole mode number,  $k_\lambda$  is the wave number,  $(R/Q)_\lambda$

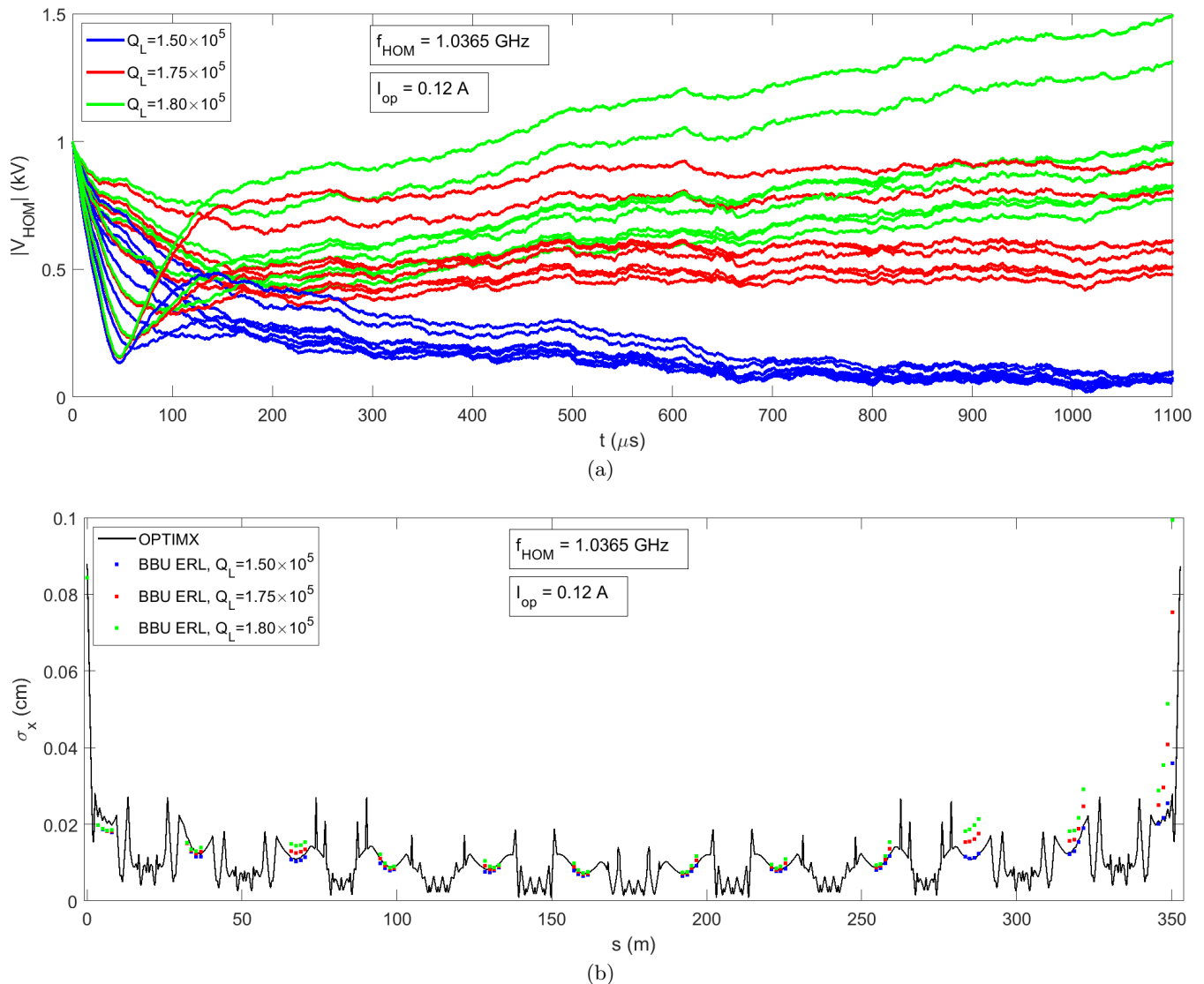


FIG. 21: PERLE BBU tracking model with 8 cavities. (a) HOM voltages when  $Q_L$  is below (blue), at (red), and above (green) the critical  $Q_L$  value and (b) corresponding RMS of beam centroid.

is the shunt impedance per unit charge,  $Q_\lambda$  is the quality factor, and  $e$  is the charge of an electron.

It can be seen that the analytical model and simulation broadly agree and follow similar trends. The lowest critical  $Q_L = 1.75 \times 10^5$  is by TE111  $4\pi/5$  mode. The other low critical  $Q_L$ s are  $3.6 \times 10^5$ ,  $3.7 \times 10^5$  and  $5.1 \times 10^5$ , which are by TE111  $3\pi/5$ , TM110  $4\pi/5$ , and TM111  $3\pi/5$  modes, respectively. These results provide the design criteria for cavity HOM dampers.

### VIII. OUTLOOK, ERL ROADMAP

PERLE - a ‘stepping stone’ to the LHeC - is designed to validate choices for a high energy ERL foreseen in the

design of the Large Hadron electron Collider (50 GeV) and the Future Circular Collider (FCC-eh, 60 GeV) [3]. PERLE is a compact ERL, resembling the LHeC configuration, based on superconducting RF technology, expands the operational regime for ERLs to 10 MW of beam power. The facility was described and recognized in 2021 as a key part of the European Roadmap towards novel accelerators [25] for its unique characteristics paving the way not only for sustainable, multi-turn ERL technology, but also for pioneering industrial and low energy physics applications. PERLE also provides the ideal test bed for the necessary SRF technology developments toward greater efficiency: fast reactive tuners to enable savings from the RF power, and Nb<sub>3</sub>Sn on copper SRF cavities to enable savings from cryogenics through 4.5 K running. Funding has been sought as part of the iSAS (Innovate for

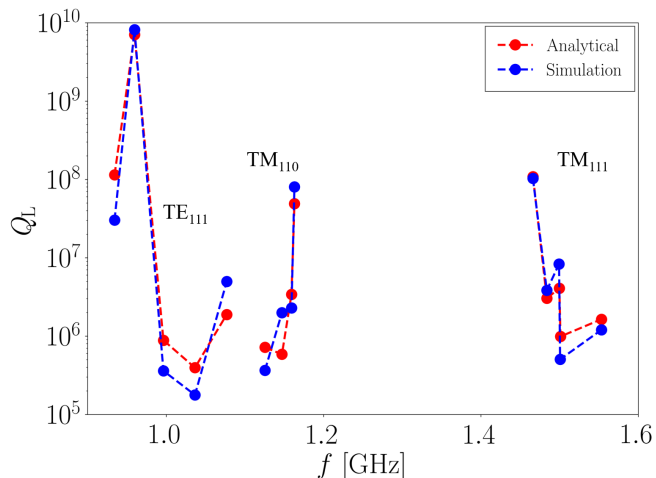


FIG. 22: Critical  $Q_L$ s for first 15 dominant HOM modes estimated in simulation and analytical model for  $I_{op} = 120$  mA.

Sustainable Accelerating Systems) proposal to develop this technology and implement it on PERLE [26]. The Large Hadron electron Collider has been designed [27] as a novel part of the LHC facility with a far reaching physics program - both for energy frontier deep inelastic electron-hadron scattering and for empowering the exploration of proton-proton and heavy ion physics

at the LHC. It builds on the complex, existing, expensive infrastructure of the LHC and represents the most economic way towards a higher precision Higgs physics program, which specifically relies on energy recovery technology at high currents. ERL is a principal means for reducing the power consumption for the next generation of lepton colliders. Operating without energy recovery, the LHeC would use GW of power. Thanks to employing the energy recovery, the net power is reduced to 100 MW or possibly below. It thus is a first large scale example of an energy efficient particle physics accelerator, for which PERLE primarily provides and tests the required technology.

## IX. ACKNOWLEDGEMENTS

Useful discussions and conceptual input from: Erk Jensen, Dario Pellegrini, Rama Calaga and Alessandra Valloni at various stages of the accelerator design process are greatly acknowledged.

## FUNDING INFORMATION

Work at Jefferson Lab has been supported by the U.S. Department of Energy, Office of Science, Office of Nuclear Physics under contracts DE-AC05-06OR23177 and DE-SC0012704.

- 
- [1] D. Angal-Kalinin *et al.*, PERLE - Powerful energy recovery linac for experiments. Conceptual design report, *Journal of Physics G: Nuclear and Particle Physics* **45**, 10.1088/1361-6471/aaa171 (2018), arXiv:1705.08783.
  - [2] A. Hutton, Energy-recovery linacs for energy-efficient particle acceleration, *Nature Reviews Physics* 10.1038/s42254-023-00644-6 (2023).
  - [3] B. J. Holzer and K. D. J. André, Energy Frontier DIS at CERN: the LHeC and the FCC-eh, in *Proceedings of 40th International Conference on High Energy physics — PoS(ICHEP2020)*, Vol. 390 (2021) p. 687.
  - [4] E. Jensen *et al.*, PERLE - a Powerful ERL Facility Concept, in *Proceedings of Nuclear Photonics Conference, Monterey, CA* (2016).
  - [5] D. Pellegrini, A. Latina, D. Schulte, and S. A. Bogacz, Beam-dynamics driven design of the LHeC energy recovery linac, *Phys. Rev. Accel. Beams* **18**, 121004 (2015).
  - [6] O. Brüning and M. Klein, *The Large Hadron-Electron Collider at the HL-LHC*, Tech. Rep. (CERN, Geneva, 2020) submitted to *J.Phys.*, arXiv:2007.14491.
  - [7] C.-Y. Tsai, S. Di Mitri, D. Douglas, R. Li, and C. Tennant, Conditions for coherent-synchrotron-radiation-induced microbunching suppression in multibend beam transport or recirculation arcs, *Phys. Rev. Accel. Beams* **20**, 024401 (2017).
  - [8] A. Fomin, L. Perrot, J. Michaud, R. Abukeshek, C. Guyot, and S. A. Bogacz, Lattice design of 250 MeV version of PERLE, in *Proc. 14th International Particle Accelerator Conference (IPAC'23)*, International Particle Accelerator Conference No. 14 (JACoW Publishing, Geneva, Switzerland, 2023).
  - [9] B. Carlsten, New photoelectric injector design for the Los Alamos National Laboratory XUV-FEL accelerator, *Nuclear Instruments and Methods in Physics Research Section A: Accelerators, Spectrometers, Detectors and Associated Equipment* **285**, 313 (1989).
  - [10] V. N. Litvinenko, R. Hajima, and D. Kayran, Merger designs for ERLs, *Nuclear Instruments and Methods in Physics Research Section A: Accelerators, Spectrometers, Detectors and Associated Equipment* **557**, 165 (2006).
  - [11] B. R. Hounsell, *Conceptual design of the PERLE injector*, Ph.D. thesis, University of Liverpool (2023).
  - [12] F. Zhou *et al.*, Experimental studies with spatial gaussian-cut laser for the LCLS photocathode gun, in *Proc. FEL2011* (Shanghai, China, 2011) pp. 341–344.
  - [13] G. Pérez Segurana, I. R. Bailey, and P. H. Williams, Construction of self-consistent longitudinal matches in multipass energy recovery linacs, *Phys. Rev. Accel. Beams* **25**, 021003 (2022), arXiv:2111.15372 [physics.acc-ph].
  - [14] S. Setiniyaz, R. Apsimon, and P. H. Williams, Implications of beam filling patterns on the design of recircu-

- lating Energy Recovery Linacs, *Phys. Rev. Accel. Beams* **23**, 072002 (2020), arXiv:2001.04156 [physics.acc-ph].
- [15] S. Setiniyaz, R. Apsimon, and P. H. Williams, Filling pattern dependence of regenerative beam breakup instability in energy recovery linacs, *Phys. Rev. Accel. Beams* **24**, 061003 (2021), arXiv:2104.13418 [physics.acc-ph].
- [16] K. D. J. André, *Lattice Design and Beam Optics for the Energy Recovery Linac of the Large Hadron-Electron Collider*, Ph.D. thesis, University of Liverpool (2023).
- [17] D. Pellegrini, *Beam dynamics studies in recirculating machines*, Ph.D. thesis, Ecole Polytechnique Fédérale de Lausanne (2016).
- [18] D. Sagan, Bmad: A relativistic charged particle simulation library, *Computational accelerator physics. Proceedings, 8th International Conference, ICAP 2004, St. Petersburg, Russia, June 29-July 2, 2004*, Nucl. Instrum. Meth. **A558**, 356 (2006), proceedings of the 8th International Computational Accelerator Physics Conference.
- [19] C. M. Lyneis, R. E. Rand, H. A. Schwettman, and A. M. Vetter, Standing wave model of regenerative beam breakup in recirculating electron accelerators, *Nucl. Instrum. Meth.* **204**, 269 (1983).
- [20] E. Pozdeyev, Regenerative multi-pass beam breakup in two dimensions, *Phys. Rev. ST Accel. Beams* **8**, 054401 (2005).
- [21] C. Tennant, *Studies of Energy Recovery Linacs at Jefferson Laboratory: 1 GeV Demonstration of Energy Recovery at CEBAF and Studies of the Multibunch, Multipass Beam Breakup Instability in the 10 kW FEL Upgrade Driver*, Ph.D. thesis, Thomas Jefferson National Accelerator Facility (TJNAF), Newport News, VA (United States) (2006).
- [22] E. Pozdeyev, C. Tennant, J. J. Bisognano, M. Sawamura, R. Hajima, and T. I. Smith, Multipass Beam Breakup in Energy Recovery Linacs, *Nucl. Instrum. Meth. A* **557**, 176 (2006).
- [23] B. C. Yunn, Expressions for the threshold current of multipass beam breakup in recirculating linacs from single cavity models, *Phys. Rev. ST Accel. Beams* **8**, 104401 (2005).
- [24] C. Barbagallo, HOM-Damping Studies in a Multi-Cell Elliptical Superconducting RF Cavity for the Multi-Turn Energy Recovery Linac PERLE, in *66th ICFA Advanced Beam Dynamics Workshop on Energy Recovery Linacs* (2022).
- [25] C. Adolphsen *et al.*, European Strategy for Particle Physics – Accelerator R&D Roadmap, CERN Yellow Rep. Monogr. **1**, 1 (2022), arXiv:2201.07895 [physics.acc-ph].
- [26] J. D’Hondt *et al.*, Innovate for sustainable accelerating systems (ISAS) (2023), proposal No. 101131435 to HORIZON-INFRA-2023-TECH-01 (European Commission, 2023).
- [27] P. Agostini *et al.* (LHeC, FCC-he Study Group), The Large Hadron–Electron Collider at the HL-LHC, *J. Phys. G* **48**, 110501 (2021), arXiv:2007.14491 [hep-ex].